A facile method for *in-situ* synthesis of SnO$_2$/graphene as a high performance anode material for lithium-ion batteries

Guiliang Wu[a], Mingbo Wu[a,*], Ding Wang[b], Linghong Yin[a], Jiashun Ye[a], Shenzhen Deng[a], Zhiyuan Zhu[a], Wenjun Ye[a], Zhongtao Li[a,*]

[a] *State Key Laboratory of Heavy Oil Processing, China University of Petroleum, Qingdao 266580, China*
[b] *School of Materials Science and Engineering, University of Shanghai for Science and Technology, Shanghai 200093, China*

ARTICLE INFO

ABSTRACT

A facile, moderate, and environment-friendly method for *in-situ* preparation of SnO$_2$/graphene nanocomposites (SnO$_2$/GNs) was proposed. The structures and morphology as well as electrochemical behaviors of SnO$_2$/GNs with varied proportions of SnO$_2$ and graphene were characterized by X-ray diffraction, Fourier transform infrared spectrometry, transmission electron microscopy and relevant electrochemical property tests. The results reveal that the ratios of SnO$_2$ to graphene have a significant effect on the structures and properties of SnO$_2$/GNs. SnO$_2$/GN-50 containing 50% SnO$_2$ delivers a high specific capacity of 540 mAh g^{-1} even after 90 cycles at a current density of 100 mA g^{-1}, which is attributed to the synergistic effect of a unique combination of SnO$_2$ nanoparticles and graphene sheets, indicating that SnO$_2$/GNs might have a promising future as anode material in Li-ion batteries.

1. Introduction

Lithium ion batteries (LIBs) as one series of important energy storage devices have been widely used in modern electronic equipment and electric/hybrid vehicles [1,2]. The theoretical capacity of graphite anode is merely 372 mAh g^{-1}, which is unable to satisfy the increasing requirement for LIBs with higher capacity. Therefore, many alternative anode materials such as metal oxide, metal sulfide, and nonmetal with larger specific capacity are explored to substitute graphite [3–7]. Tin dioxide (SnO$_2$) is regarded as one of most promising anode materials for the next-generation LIBs due to its high theoretical capacity (782 mAh g^{-1}), low cost and nontoxicity [8–10]. However, SnO$_2$ suffers from severe volume change during Li$^+$ insertion/extraction process, which has been the biggest challenge for SnO$_2$ as LIBs anode in practical applications [11,12]. Designing SnO$_2$ nanostructures, such as core-shell structures [13,14], hollow structures [15], nanotubes [16], nanowires [17], and nanorods [18], is an effective way to mitigate the volume expansion. Hybridizing SnO$_2$ with buffer materials (such as carbon or other conductive materials) is another strategy to accommodate volume variation [19–21]. Nonetheless, the above mentioned preparation processes are usually complicated

and time-consuming. Therefore, it is in urgently need of a facile and efficient method to synthesize SnO$_2$-based anode materials.

Graphene (GN) with superior electronic conductivity, high surface area, and chemical and physical stabilities [22,23] has been served as functional substrate to hybridize with SnO$_2$ for improving capacity and cyclic stability of the anode materials [9,24–26]. Herein, SnO$_2$/GN composites with different morphology and structure have been synthesized by various techniques. Yao et al. prepared SnO$_2$/GN composites via a reflux approach in an oil bath at 120 °C and calcined at 300 °C for 10 h subsequently [24]. The obtained sample exhibits a reversible capacity of 520 mAh g^{-1} after 100 cycles at a rate of 55 mA g^{-1}. Liang et al. synthesized the SnO$_2$/GN nanocomposites by a reflux method at 180 °C for 10 h [25]. The as-prepared sample followed by calcination at 400 °C shows a capacity of 430 mAh g^{-1} after 20 cycles at a current density of 100 mA g^{-1}. Park and co-workers developed a hydrothermal method to prepare SnO$_2$/GN materials [27]. Although the as-made sample prepared at 160 °C for 12 h in hydrazine monohydrate delivers a high reversible capacity of 626 mAh g^{-1} after 50 cycles at a rate of 100 mA g^{-1}, its preparation process is generally complex, harsh, and time-consuming.

To solve the above problems, we propose a facile, moderate, and efficient method for *in-situ* preparation of SnO$_2$/GNs without adding any toxic chemicals. The effects of the ratios of SnO$_2$ to graphene on the structures as well as electrochemical behaviors are also systematically investigated.

* Corresponding authors. Tel.: +86 532 8698 3452.
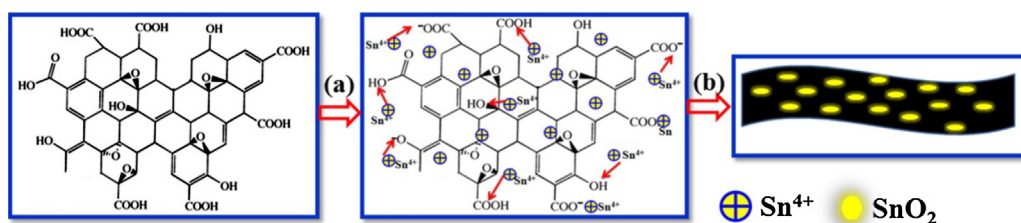*E-mail addresses:* wumb@upc.edu.cn (M. Wu), liztao@upc.edu.cn (Z. Li).

Fig. 1. Synthetic procedure of SnO$_2$/GNs. (For interpretation of the references to color in this figure legend, the reader is referred to the web version of the article.)

2. Experimental

2.1. Chemical reagents and materials

Graphite powder (325 mesh, with purity >99.99%) was obtained from Alfa Aesar. All the other chemicals (AR, Sinopharm Chemical Reagent Co., Ltd.) in our experiment were directly used without further purification.

2.2. Synthesis of SnO$_2$/GNs

Graphene oxide (GO) was gained from graphite powder by a modified Hummers' method [28], followed by sonication (700 W) for 4 h in distilled water. Different amounts of SnCl$_4$·5H$_2$O were dissolved in 200 mL GO suspension (1 mg mL^{-1}) along with vigorously stirring. Afterwards, its pH value was adjusted among 9–10 by injecting ammonia (25.0–38.0 wt%). The mixture was stirred sufficiently in a water bath for 2 h at 85 °C, leading to a light black suspension solution. The resultant solid products were separated by filtration, washed with distilled water, and dried in vacuum at 60 °C. Finally, the products were obtained after calcining at 500 °C for 2 h in N$_2$ atmosphere and remarked as SnO$_2$/GNs. The contents of SnO$_2$ in different samples are estimated by the following formula:

$$SnO_2\% = \frac{m_{SnO_2}}{\left(m_{GO} + m_{SnO_2}\right)} \qquad (1)$$

According to the formula, SnO$_2$% of SnO$_2$/GN-30, SnO$_2$/GN-50 and SnO$_2$/GN-70 are 30%, 50% and 70%, respectively.

2.3. Samples characterization

The structure and morphology of obtained SnO$_2$/GNs were analyzed by X-ray diffraction (XRD, X'Pert PRO MPD, Holland), and transmission electron microscopy (TEM, JEM-2100UHR, Japan). The functional groups in samples were characterized by Fourier transform infrared spectrometry (FT-IR, Thermo Nicolet NEXUS 670, USA). The contents of SnO$_2$ in samples were quantitatively determined by thermogravimetric analysis (TGA, STA 409 PC Luxx, Germany). Raman analysis was performed with a Jobin Yvon HR800 Raman spectrometer. Brunauer–Emmet–Teller (BET) specific surface area was determined from nitrogen adsorption/desorption isotherms using automatic specific surface area measuring equipment (ASAP 2020, America).

2.4. Electrochemical measurements

Working electrodes were prepared from SnO$_2$/GNs, carbon black and poly(vinylidene fluoride) (8:1:1 in weight ratio) in N-methyl-2-pyrrolidinone. The slurry was coated onto a current collector made from copper foil and then was dried under vacuum at 100 °C for 10 h. The cells were assembled inside an argon-filled glove box using a lithium-metal foil as the counter electrode and microporous polypropylene as the separator. The organic electrolyte was composed of 1 mol L^{-1} LiPF$_6$ in ethylene carbonate and diethyl carbonate (EC/DMC, 1:1 vol). The cells were galvanostatically charged and discharged in the voltage range from 0.005 to 2.5 V vs. Li/Li$^+$ at the current density of 100 mA g^{-1} on a Land CT2001A cycler. Cyclic voltammetry (CV) curves were collected at 0.25 mV s^{-1} with in the range of 0.005–2.5 V using an Ametek PARSTAT4000 electrochemistry workstation. Electrochemical impedance spectroscopy (EIS) tests were also measured on Ametek PARSTAT4000 electrochemistry workstation in the frequency range of 100 kHz to 10 mHz with AC voltage amplitude of 10 mV.

3. Results and discussion

Fig. 1 reveals the overall *in-situ* synthesis of SnO$_2$/GNs. The abundant functional groups on the surface of GO, such as epoxy, hydroxyl, and carboxyl groups [29], can act as anchoring sites for Sn^{4+} through electrostatic interactions. When SnCl$_4$·5H$_2$O was added into GO solution, Sn^{4+} was regularly combined with the oxygenated groups by electrostatic attraction (*cf. red arrows*). The bonded Sn^{4+} could quickly move to active sites on GO planes under violently stirring at 85 °C and then in situ convert into Sn(OH)$_4$ on the GO sheets as soon as ammonia was injected into reaction system. After reacted at 85 °C for 2 h, the mixture became light black, which could be attributed to the partial reduction of GO under this reaction temperature by ammonia. Finally, Sn(OH)$_4$ deposited on GO sheets was converted to SnO$_2$ particles (*cf. yellow dots*) after calcining at 500 °C for 2 h in N$_2$. Simultaneously, GO was further reduced to graphene. SnO$_2$ nanoparticles (NPs) uniformly disperse on graphene sheets and finally form the final SnO$_2$/GNs.

XRD patterns of SnO$_2$/GNs are shown in Fig. 2. The peak around 11°, a characteristic diffraction peak of graphite oxide, cannot be observed in SnO$_2$/GN samples, indicating that graphite oxide has been well exfoliated. In addition, the peak of SnO$_2$ (1 1 0) plane around 26° is asymmetric, which is ascribed to the overlapping
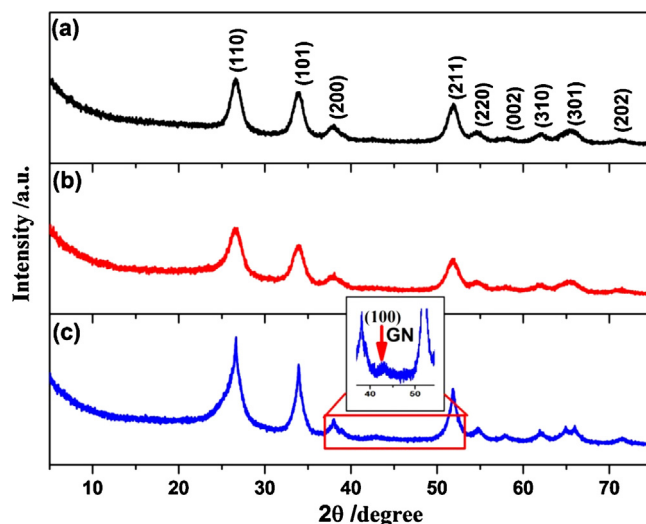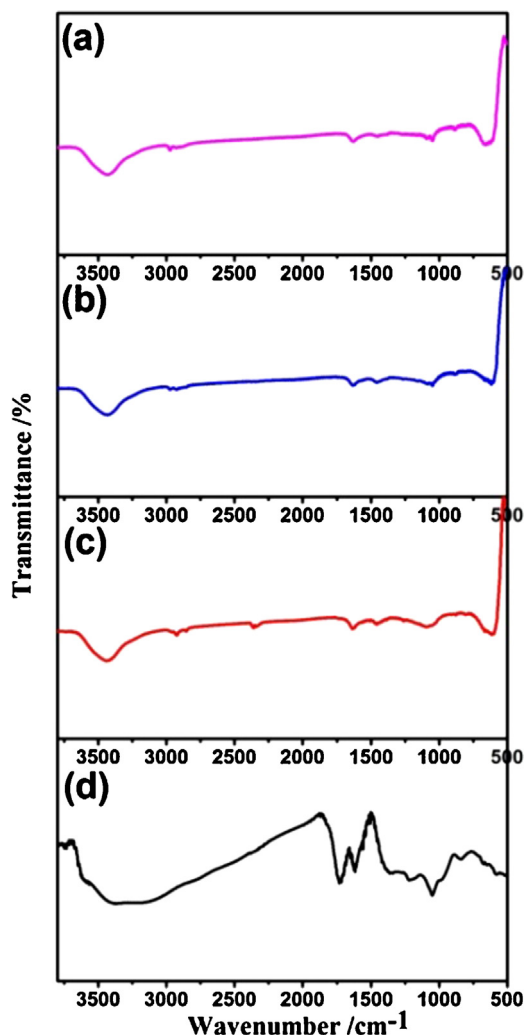

Fig. 2. XRD patterns of SnO$_2$/GNs.

Fig. 3. FT-IR spectra of SnO_2/GNs and GO.

Fig. 4. Raman spectra of SnO_2/GNs and GO.

of the reduced graphene sheets reflection with the most intense (1 1 0) reflection of the cassiterite structure. As we can see, all three SnO_2/GN samples exhibit four distinct diffraction peaks (1 1 0), (1 0 1), (2 1 1), and (3 0 1), which are attributed to the tetragonal rutile SnO_2 phase (Cassiterite, JCPDS card No. 41-1445). These broad peaks of SnO_2/GNs indicate that the SnO_2 NPs in SnO_2/GNs are very small in size [9,27]. Based on the Scherrer's formula, the average crystallite sizes for SnO_2/GN-30, SnO_2/GN-50 and SnO_2/GN-70 are 4.5, 8.1, 13.5 nm, respectively. With the increasing content of SnO_2, the estimated size of SnO_2 NPs in SnO_2/GN samples becomes much larger, which also has been approved by TEM (in Fig. 6). It should be noted that a weak diffraction peak around 43° can be detected only in SnO_2/GN-30, as shown in the inset of Fig. 2(c), indicating that more graphene sheets (ca.70% according to the equation (1)) in SnO_2/GN-30 stack with each other and form into multilayers by the van der Waals forces. However, the relevant diffraction peaks are not found in SnO_2/GN-50 and SnO_2/GN-70, revealing that the higher amounts of SnO_2 NPs deposited on graphene sheets can prevent the latter from stacking into multilayers [30].

To make sure the reduction of GO during the preparation of SnO_2/GNs, FT-IR spectra of SnO_2/GNs and GO were measured, as revealed in Fig. 3. Many oxygen-containing groups including C–OH (3390 cm^{-1}), C–O–C (1230 cm^{-1}), and C=O (1735 cm^{-1}) in COOH can be detected on the FT-IR spectrum of GO (Fig. 3(d)). The spectrum of GO also shows the O–H deformation peak at 1401 cm^{-1}, the C–O stretching peak at 1055 cm^{-1}, and the O–C=O
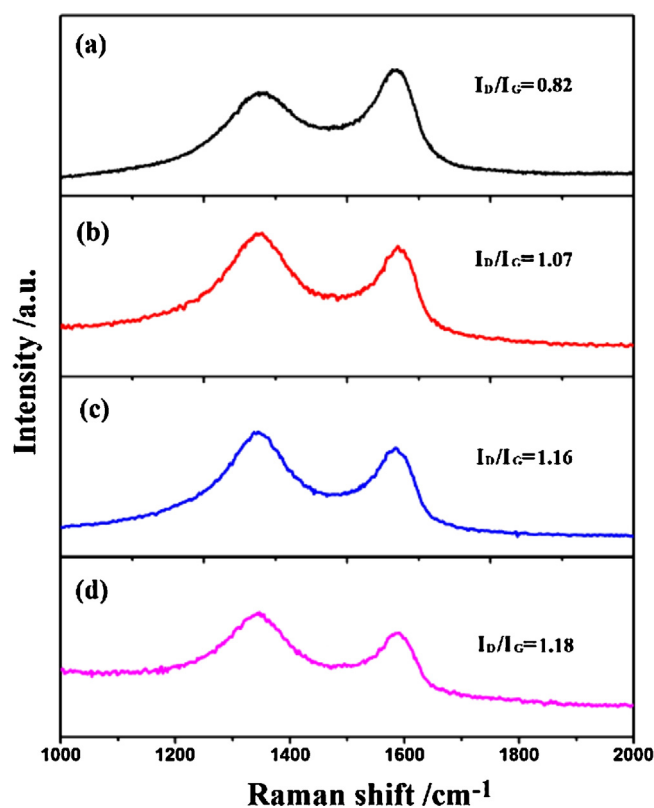
at 830 cm^{-1}. In addition, a peak at 1620 cm^{-1} can be attributed to the remaining sp^2 domains [31]. The FT-IR spectra of SnO_2/GN-70, SnO_2/GN-50, and SnO_2/GN-30 exhibit a similar trend: most of the peaks of oxygen-containing groups, such as COOH peaks (1735 cm^{-1}), C–O stretching vibrations (1055 cm^{-1}), O–H deformation peak (1401 cm^{-1}), and O–C=O peak (830 cm^{-1}), are eliminated after calcination at 500 °C. Furthermore, the peaks of C–OH at 3390 cm^{-1} of all three SnO_2/GN samples are much weaker compared with GO, and the new strong peaks at 600 cm^{-1} assigned to Sn–O are appeared. All these results prove that most GO has been reduced to graphene and Sn^{4+} has been transformed into SnO_2.

Raman spectroscopy measurement was carried out to characterize GO and SnO_2/GNs. As shown in Fig. 4(a), the Raman spectrum of GO contains both G (1580 cm^{-1}) and D (1350 cm^{-1}) bands, corresponding to sp^2 hybridized carbon and the disordered carbon, respectively [32]. All three SnO_2/GN samples also exhibit the two bands in Raman spectra. However, the intensity ratios of the D to the G band (I_D/I_G) of SnO_2/GN samples (1.07, 1.16, and 1.18 for SnO_2/GN-30, SnO_2/GN-50, and SnO_2/GN-70, respectively) are higher than 0.82 of GO, and the value becomes larger with the increasing Sn^{4+}/GO ratio, which is due to the decreasing amount of exfoliated GO [9,33], as well as the increasing amount of SnO_2 NPs deposited on the graphene sheets [34].

The contents of SnO_2 in SnO_2/GNs were estimated by the thermogravimetric analysis in air, as revealed in Fig. 5. For all SnO_2/GN samples, the major weight loss steps in the range of 200–650 °C can be easily seen, which are attributed to the gradually oxidation of graphene in air. Based on the TGA curves, the mass percent of SnO_2 is 77.6, 56.0, and 40.8% in SnO_2/GN-70, SnO_2/GN-50, and SnO_2/GN-30, respectively. The final contents of SnO_2 in above three samples are relatively higher than 70, 50, 30% of theoretical values according to formula (1), which is caused by the removal of oxygen-containing groups in GO during the calcining processes.
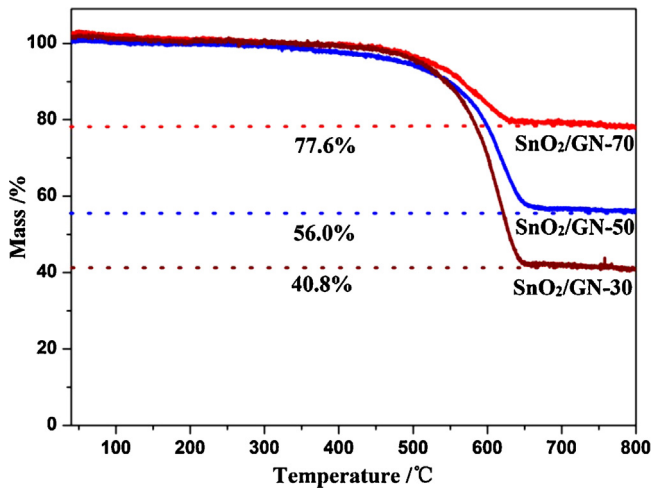
Fig. 5. TGA curves of SnO$_2$/GNs in air.

of SnO$_2$, respectively. As we all know, the monolayer graphene looks like a wrinkled or crumpled thin paper-like structure with a lot of folds at the edge due to its intrinsic properties [35]. Interestingly, the surface of graphene in SnO$_2$/GN-30 is relatively smooth compared with other two samples. It is presumed that GO exfoliated by sonication in SnO$_2$/GN-30 reassemble into multilayer graphene during the preparation process.

High-resolution (HR) TEM images of all three SnO$_2$/GN samples were further performed, as depicted in Fig. 7. The layer amount of stacking graphene in SnO$_2$/GN-30 are 8–10 layers, which can be approximately counted from the number of strips as marked with arrows in Fig. 7(a). The layers of graphene in SnO$_2$/GN-50 and SnO$_2$/GN-70 are distinguished by the same means, which are 2–3 and 3–5 layers, respectively. As shown in the pictures, the graphene sheets can effectively prevent the aggregation of SnO$_2$ NPs, thereby form a well dispersed SnO$_2$ NPs in SnO$_2$/GNs. Meanwhile, the SnO$_2$ NPs deposited on graphene sheets can also restrain graphene sheets from stacking into multilayers [30]. The more stacking of graphene sheets in SnO$_2$/GN-30 rather than those in SnO$_2$/GN-50 and SnO$_2$/GN-70 is due to the poor loading of SnO$_2$ NPs (*ca.* 40%), which is in accordance with the results of XRD. The morphology and structure of SnO$_2$/GN nanocomposites seem to be highly related with the ratio of Sn^{4+}/GO.

The nitrogen adsorption/desorption isotherms of SnO$_2$/GNs together with the pore size distribution are shown in Fig. 8. All three samples exhibit the typical type IV isotherm with an obvious hysteresis loop, suggesting that a certain amount of mesopores actually exist in SnO$_2$/GNs [36]. The specific surface area of SnO$_2$/GN-30, SnO$_2$/GN-50, and SnO$_2$/GN-70 is 89.7, 97.4, and 124.6 m^2 g^{-1}, respectively. Although SnO$_2$/GN-70 possesses the largest surface area, however, SnO$_2$/GN-70 does not show the best electrochemical properties (see Fig. 10), which could be attributed that the aggregated SnO$_2$ NPs in SnO$_2$/GN-70 (see Fig. 6(d)) are not beneficial for the fast Li-ion diffusion.
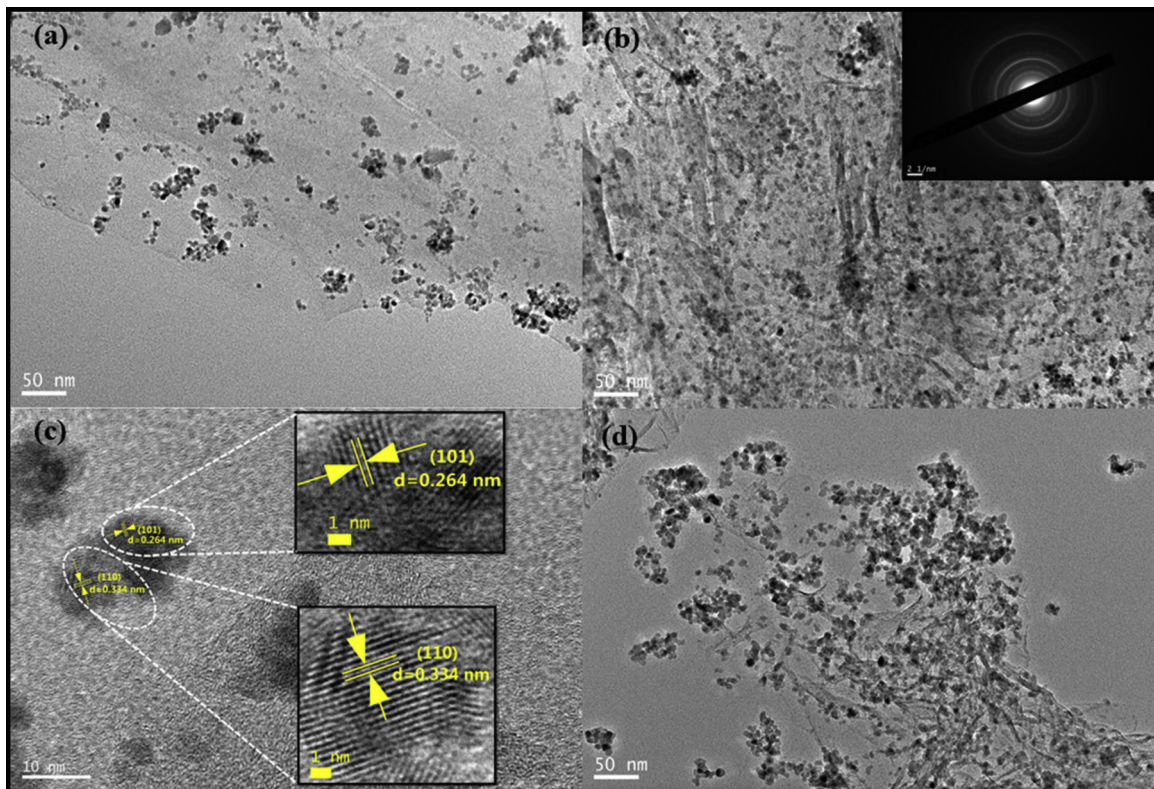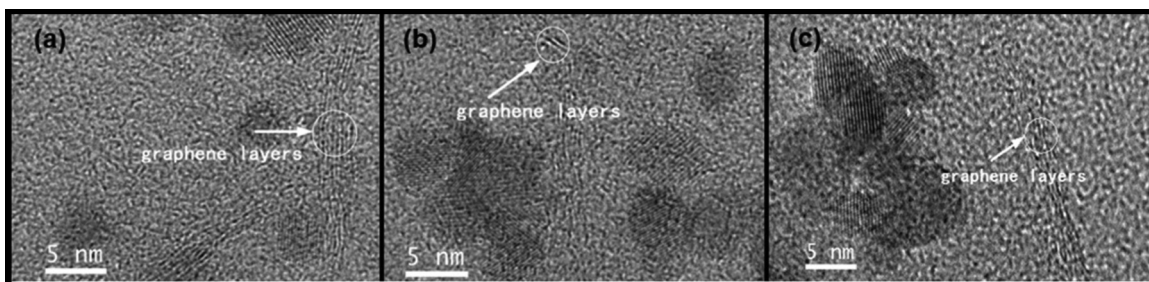
The morphology and structural features of SnO$_2$/GNs were characterized by TEM. As shown in Fig. 6, the SnO$_2$ NPs distributed on the surface of graphene planes can be clearly observed in all SnO$_2$/GN samples. The difference is that SnO$_2$ NPs in SnO$_2$/GN-50 (Fig. 6(b)) are uniformly distributed. However, SnO$_2$ NPs in SnO$_2$/GN-30 (Fig. 6(a)) are sporadically dispersed, and those in SnO$_2$/GN-70 are obviously aggregated into larger particles as shown in Fig. 6(d). The corresponding selected-area electron diffraction (SAED) pattern (inset of Fig. 6(b)) exhibits distinct diffraction rings indexed to tetragonal rutile SnO$_2$ nanocrystal phase. Furthermore, the lattice fringes of SnO$_2$ NPs are clearly observed in Fig. 6(c) and its insets. The interlayer spacings are about 0.334 nm and 0.264 nm, corresponding to (1 1 0) and (1 0 1) planes

Fig. 6. TEM images of SnO$_2$/GNs.

Fig. 7. HRTEM images of SnO$_2$/GNs.

Fig. 8. Nitrogen adsorption/desorption isotherms of SnO$_2$/GNs.
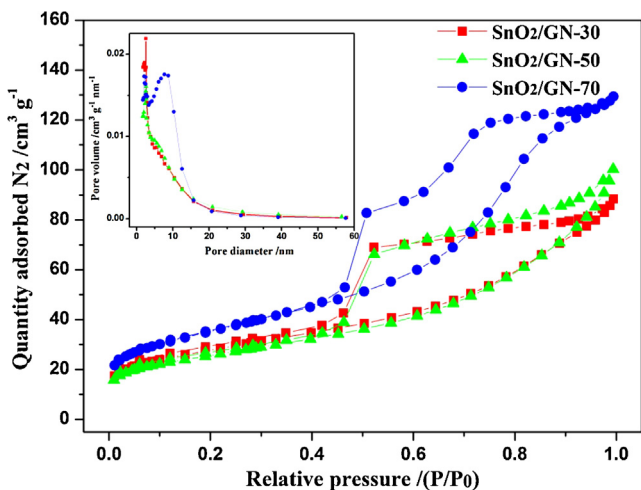
Fig. 10. The cyclic performances of SnO$_2$/GNs.

The electrochemical performance of SnO$_2$/GNs as anodes of LIBs shown in Figs. 9 and 10 were investigated by galvanostatic discharge/charge tests in the voltage range of 0.005–2.5 V (vs. Li/Li$^+$) at a current density of 100 mA g^{-1}. For comparison, discharge/charge cycling of pure SnO$_2$ was carried out in the same conditions. Fig. 9(a) shows the discharge/charge voltage profiles of SnO$_2$/GN-50 for the 1st, 2nd, and 10th cycles. A classical plateau around 0.8 V can
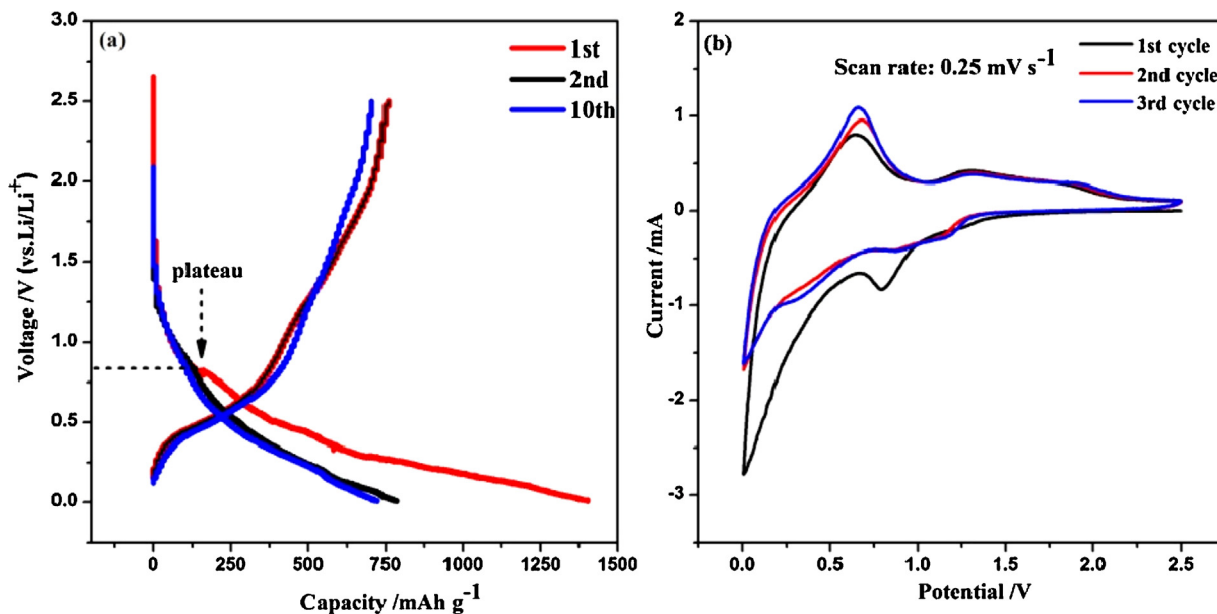
be found only in the first cycle, corresponding to the reaction of SnO$_2$ with lithium to form amorphous lithium oxide (Li$_2$O) and the formation of a solid electrolyte interface (SEI) layer [24,37]. SnO$_2$/GN-50 exhibits a discharge capacity of 1402 mAh g^{-1} and a reversible capacity of 750 mAh g^{-1} in first cycle. The initial coulombic efficiency is low (about 54%), indicating the larger irreversible capacity loss due to the formation of Li$_2$O and SEI film. To better illustrate the mechanism of the electrochemical reaction happened in SnO$_2$/GNs, the cyclic voltammogram (CV) of SnO$_2$/GN-50 was

Fig. 9. (a) Charge/discharge profiles and (b) the cyclic voltammogram of SnO$_2$/GN-50.

performed at a scan rate of 0.25 mV s^{-1} in the voltage range of 0.005–2.5 V, as shown in Fig. 9(b). A dominant irreversible reduction peak at 0.8 V in the initial cycle is observed, corresponding to the reduction of SnO_2 to Li_2O and Sn (Eq. (2)) and the formation of SEI layer. The clearly cathodic peak around 0.02 V and the anodic peak around 0.68 V are related to the reversible alloying/de-alloying reactions between Sn and Li (Eq. (3)) [10]. From the second cycle, the new cathodic peaks appeared at 0.45 V and 1.0–1.2 V could be attributed to the formation of different phases of Li–Sn alloy such as $Li_{13}Sn_5$, Li_5Sn_2 and LiSn [38,39]. Meanwhile, the anodic peak at 1.3 V could correspond to the de-alloying process of certain phases of Li_xSn [38,39].

$$SnO_2 + 4Li^+ + 4e^- \rightarrow 2Li_2O + Sn \qquad (2)$$

$$Sn + xLi^+ + xe^- \leftrightarrow Li_xSn \quad (0 \leq x \leq 4.4) \qquad (3)$$
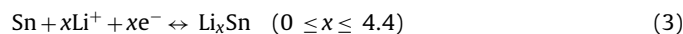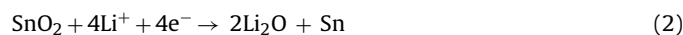
The cycling performances of SnO_2/GN-30, SnO_2/GN-50, SnO_2/GN-70 and pure SnO_2 are shown in Fig. 10. As expected, all three SnO_2/GN samples present good cycling stabilities, and the discharge capacities are 417, 603, and 522 mAh g^{-1} after 50 cycles for SnO_2/GN-30, SnO_2/GN-50, and SnO_2/GN-70, respectively. However, the pure SnO_2 capacity quickly drops to 224 mAh g^{-1} after 50 cycles due to the large volume expansion during the cycling. These results indicate that the method of depositing SnO_2 on the graphene sheets can effectively alleviate the volume variation, and improve their electrochemical properties.

It is worth noting that SnO_2/GN-50 still delivers a higher discharge capacity than SnO_2/GN-30 and SnO_2/GN-70, which can keep a stable capacity of 540 mAh g^{-1} even after 90 cycles for SnO_2/GN-50. In addition, the relevant coulombic efficiencies of SnO_2/GN-50 stay around 100% after several cycles, indicating the good electrochemical reversibility of SnO_2/GN-50. The superior electrochemical performance of SnO_2/GN-50 can be ascribed to the synergistic effect of a unique combination of SnO_2 NPs and graphene sheets, i.e. the SnO_2 NPs dispersed on the graphene sheets can effectively relieve the volume changes as well as the aggregation of SnO_2 NPs during cycling process. Meanwhile, the SnO_2 NPs deposited on graphene sheets can also keep them from stacking back to the multilayer. SnO_2/GN-30 with less SnO_2 NPs shows an inferior electrochemical performance due to the re-stacking of graphene sheets. In contrast, the cycling stability of SnO_2/GN-70 with more deposited SnO_2 is also poor, which is due to the aggregation of SnO_2 NPs on the graphene surfaces. In conclusion, the proportions of SnO_2 and graphene have a significant effect on the structures as well as electrochemical behaviors of synthesized SnO_2/GNs. Therefore, to obtain SnO_2/GNs with best electrochemical performance, the Sn^{4+}/GO ratio should be fine-tuned in appropriate range.

Fig. 11(a) shows the rate capability of SnO_2/GN-50 at the current densities of 100, 200, and 400 mA g^{-1}. SnO_2/GN-50 delivers a high capacity of 402 mAh g^{-1} even at a high rate of 400 mA g^{-1}, which is still much higher than 372 mAh g^{-1} of graphite. Moreover, the capacity of SnO_2/GN-50 rebounds back to near 500 mAh g^{-1} when the current density swings back to 100 mA g^{-1}, indicating that SnO_2/GN-50 possesses better rate performance.

To further evaluate the electrochemical performances of SnO_2/GNs and SnO_2, electrochemical impedance spectroscopy (EIS) tests were performed. Nyquist plots of pure SnO_2 and SnO_2/GNs in Fig. 11(b) present a depressed semicircle in high-middle frequency and an inclined line in low frequency, corresponding to the charge transfer resistance and the Warburg impedance, respectively [34]. The semicircle diameters of SnO_2/GNs, especially for SnO_2/GN-50, are smaller than that of pure SnO_2, indicating enhanced electron and lithium ion transfer rates. The quick charge transfer in SnO_2/GNs leads to their superior electrochemical performances.
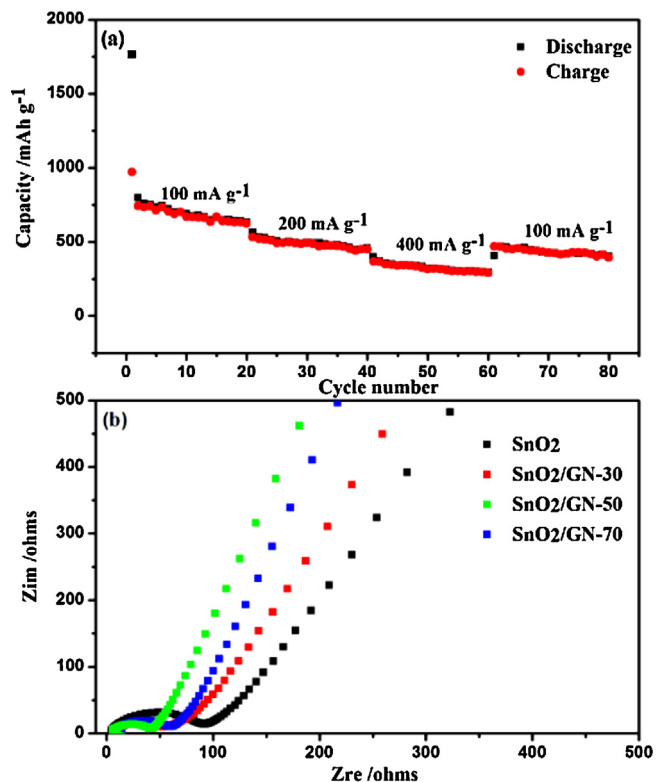

Fig. 11. (a) Rate performance of SnO_2/GN-50 and (b) electrochemical impedance spectra of SnO_2/GNs.

4. Conclusion

In this work, a facile hydrothermal technique for *in-situ* synthesis of SnO_2/GNs is proposed. Generally speaking, the preparation process of SnO_2/GNs is moderate, time-saving and toxic free. The ratio of Sn^{4+} to GO is found playing an important role on the SnO_2/GNs structures as well as the electrochemical behaviors. SnO_2/GN-50 exhibits a stable capacity of 540 mAh g^{-1} and almost 100% of coulombic efficiency even after 90 cycles. The excellent electrochemical performance of SnO_2/GN-50 can be explained to the synergistic effect of a unique combination of SnO_2 NPs and graphene sheets. The graphene sheets can effectively accommodate volume variation as well as the aggregation of SnO_2 NPs, and the SnO_2 NPs deposited on graphene sheets can also restrain the graphene sheets from stacking back the multilayer. The method described in this paper may provide a simple, economic and environment-friendly technique for the preparation of metal oxide/graphene nanocomposites.

References

[1] J.M. Tarascon, M. Armand, Nature 414 (2001) 359–367.
[2] M.H. Liang, L.J. Zhi, J. Mater. Chem. 19 (2009) 5871–5878.
[3] W.L. Wang, V.H. Nguyen, H.-B. Gu, Appl. Surf. Sci. 288 (2014) 742–746.
[4] C.K. Chan, H.L. Peng, G. Liu, K. Mcllwrath, X.F. Zhang, R.A. Huggins, Y. Cui, Nat. Nanotechnol. 3 (2008) 31–35.
[5] J.S. Zhu, D.L. Wang, T.F. Liu, Appl. Surf. Sci. 282 (2013) 947–953.

[6] A.S. Arico, P. Bruce, B. Scrosati, J.M. Tarascon, V.W. Schalkwijk, Nat. Mater. 4 (2005) 366–377.
[7] H.D. Liu, J.M. Huang, X.L. Li, J. Liu, Y.X. Zhang, K. Du, Appl. Surf. Sci. 258 (2012) 4917–4921.
[8] X.W. Lou, Y. Wang, C.L. Yuan, J.Y. Lee, L.A. Archer, Adv. Mater. 18 (2006) 2325–2329.
[9] Y. Li, X. Lv, J. Lu, J. Li, J. Phys. Chem. C 114 (2010) 21770–21774.
[10] Y. Chen, B.H. Song, R.M. Chen, L. Lu, J.M. Xue, J. Mater. Chem. A 2 (2014) 5688–5695.
[11] D. Larcher, S. Beattie, M. Morcrette, K. Edstroem, J.C. Jumas, J.M. Tarascon, J. Mater. Chem. 17 (2007) 3759–3772.
[12] M. Winter, J.O. Besenhard, Electrochim. Acta 45 (1999) 31–50.
[13] W.M. Zhang, J.S. Hu, Y.G. Guo, S.F. Zheng, L.S. Zhong, W.G. Song, L.J. Wan, Adv. Mater. 20 (2008) 1160–1165.
[14] D. Deng, J.Y. Lee, Chem. Mater. 20 (2008) 1841–1846.
[15] S.J. Han, B.C. Jang, T. Kim, S.M. Oh, T. Hyeon, Adv. Funct. Mater. 15 (2005) 1845–1850.
[16] Y. Wang, J.Y. Lee, H.C. Zeng, Chem. Mater. 17 (2005) 3899–3903.
[17] N.H. Zhao, G.J. Wang, Y. Huang, B. Wang, B.D. Yao, Y.P. Wu, Chem. Mater. 20 (2008) 2612–2614.
[18] Y. Wang, J.Y. Lee, J. Phys. Chem. B 108 (2004) 17832–17837.
[19] X.W. Lou, J.S. Chen, P. Chen, L.A. Archer, Chem. Mater. 21 (2009) 2868–2874.
[20] L. Yuan, K. Konstantinov, G.X. Wang, H.K. Liu, S.X. Dou, J. Power Sources 146 (2005) 180–184.
[21] Z.H. Wen, Q. Wang, Q. Zhang, J.H. Li, Adv. Funct. Mater. 17 (2007) 2772–2778.
[22] K.S. Novoselov, A.K. Geim, S.V. Morozov, D. Jiang, Y. Zhang, S.V. Dubonos, I.V. Grigorieva, A.A. Firsov, Science 306 (2004) 666–669.
[23] A.K. Geim, K.S. Novoselov, S.V. Morozov, D. Jiang, M.I. Katsnelson, I.V. Grigorieva, S.V. Dubonos, A.A. Firsov, Nature 438 (2005) 197–200.
[24] J. Yao, X.P. Shen, B. Wang, H.K. Liu, G.X. Wang, Electrochem. Commun. 11 (2009) 1849–1852.
[25] J.F. Liang, W. Wei, D. Zhong, Q.L. Yang, L.D. Li, L. Guo, ACS Appl. Mater. Interfaces 4 (2012) 454–459.
[26] B. Lee, S.C. Han, M. Oh, M.S. Lah, K.S. Sohn, M. Pyo, Electrochim. Acta 113 (2013) 149–155.
[27] S.K. Park, S.H. Yu, N. Pinna, S. Woo, B. Jang, Y.H. Chung, Y.H. Cho, Y.E. Sung, Y.Z. Piao, J. Mater. Chem. 22 (2012) 2520–2525.
[28] W.S. Hummers, R.E. Offeman, J. Am. Chem. Soc. 80 (1958) 1339.
[29] S. Stankovich, D.A. Dikin, G.H.B. Dommett, K.M. Kohlhaas, E.Z. Zimney, E.A. Stach, R.D. Piner, S.T. Nguyen, R.S. Ruoff, Nature 442 (2006) 282–286.
[30] P.C. Lian, X.F. Zhu, S.Z. Liang, Z. Li, W.S. Yang, H.H. Wang, Electrochim. Acta 56 (2011) 4532–4539.
[31] Y.Y. Liang, D.Q. Wu, X.L. Feng, K. Müllen, Adv. Mater. 21 (2009) 1679–1683.
[32] Z.H. Ni, H.M. Wang, J. Kasim, H.M. Fan, T. Yu, Y.H. Wu, Y.P. Feng, Z.X. Shen, Nano Lett. 7 (2007) 2758–2763.
[33] F. Tuinstra, J.L. Koenig, J. Chem. Phys. 53 (1970) 1126–1130.
[34] C.F. Zhang, X. Peng, Z.P. Guo, C.B. Cai, Z.X. Chen, D. Wexler, S. Li, H.K. Liu, Carbon 50 (2012) 1897–1903.
[35] J.C. Meyer, A.K. Geim, M.I. Katsnelson, K.S. Novoselov, T.J. Booth, S. Roth, Nature 446 (2007) 60–63.
[36] X. Sun, M. Xie, G.K. Wang, H.T. Sun, A.S. Cavanagh, J.J. Travis, S.M. George, J. Lian, J. Electrochem. Soc. 159 (2012) A364–A369.
[37] M.S. Park, Y.M. Kang, G.X. Wang, S.X. Dou, H.K. Liu, Adv. Funct. Mater. 18 (2008) 455–461.
[38] J. Song, M.Z. Cai, Q.F. Dong, M.S. Zheng, Q.H. Wu, S.T. Wu, Electrochim. Acta 54 (2009) 2748–2753.
[39] W.L. Wang, V.H. Nguyen, E.M. Jin, H.B. Gu, Mater. Express 3 (2013) 273–279.